

Article

Transition Metal Sensing with Nitrogenated Holey Graphene: A First-Principles Investigation

Uroosa Sohail ¹, Faizan Ullah ¹ , Nur Hazimah Binti Zainal Arfan ², Malai Haniti Sheikh Abdul Hamid ², Tariq Mahmood ^{1,3}, Nadeem S. Sheikh ^{2,*}  and Khurshid Ayub ^{1,*}

¹ Department of Chemistry, COMSATS University Islamabad, Abbottabad Campus, Abbottabad 22060, Pakistan; uroosasohail6666@gmail.com (U.S.); faizan@faizanullah.com (F.U.); mahmood@cuatd.edu.pk (T.M.)

² Chemical Sciences, Faculty of Science, Universiti Brunei Darussalam, Jalan Tungku Link, Gadong BE1410, Brunei; 22m1432@ubd.edu.bn (N.H.B.Z.A.); haniti.hamid@ubd.edu.bn (M.H.S.A.H.)

³ Department of Chemistry, College of Science, University of Bahrain, Isa Town 32038, Bahrain

* Correspondence: nadeem.sheikh@ubd.edu.bn (N.S.S.); khurshid@cuatd.edu.pk (K.A.)

Abstract: The toxicity of transition metals, including copper(II), manganese(II), iron(II), zinc(II), hexavalent chromium, and cobalt(II), at elevated concentrations presents a significant threat to living organisms. Thus, the development of efficient sensors capable of detecting these metals is of utmost importance. This study explores the utilization of two-dimensional nitrogenated holey graphene (C₂N) nanosheet as a sensor for toxic transition metals. The C₂N nanosheet's periodic shape and standard pore size render it well suited for adsorbing transition metals. The interaction energies between transition metals and C₂N nanosheets were calculated in both gas and solvent phases and were found to primarily result from physisorption, except for manganese and iron which exhibited chemisorption. To assess the interactions, we employed NCI, SAPT0, and QTAIM analyses, as well as FMO and NBO analysis, to examine the electronic properties of the TM@C₂N system. Our results indicated that the adsorption of copper and chromium significantly reduced the HOMO–LUMO energy gap of C₂N and significantly increased its electrical conductivity, confirming the high sensitivity of C₂N towards copper and chromium. The sensitivity test further confirmed the superior sensitivity and selectivity of C₂N towards copper. These findings offer valuable insight into the design and development of sensors for the detection of toxic transition metals.

Keywords: nitrogenated holey graphene; sensors; density functional theory; QTAIM; electronic properties



Citation: Sohail, U.; Ullah, F.; Binti Zainal Arfan, N.H.; Abdul Hamid, M.H.S.; Mahmood, T.; Sheikh, N.S.; Ayub, K. Transition Metal Sensing with Nitrogenated Holey Graphene: A First-Principles Investigation.

Molecules **2023**, *28*, 4060.

<https://doi.org/10.3390/molecules28104060>

Academic Editor: Shiru Lin

Received: 11 March 2023

Revised: 25 April 2023

Accepted: 4 May 2023

Published: 12 May 2023



Copyright: © 2023 by the authors. Licensee MDPI, Basel, Switzerland. This article is an open access article distributed under the terms and conditions of the Creative Commons Attribution (CC BY) license (<https://creativecommons.org/licenses/by/4.0/>).

1. Introduction

First row transition metals (Sc, Ti, Vn, Cr, Mn, Fe, Co, Ni, Cu and Zn) play undeniable role in various disciplines which include medicine, construction, catalysis, nuclear processes, engineering, and numerous medical applications [1–3]. One of the major application accounts for their catalytic properties in isomerization, hydrogenation, oxidation, polymerization and building small molecules, etc. [4,5] In a biological system, transition metals are associated with most of proteins to perform number of enzymatic processes and transportation to their target [6]. However, high concentration causes toxicity and is hazardous to life [7]. All elements of the series have some level of toxicity, but some are highly toxic while others are moderate [8,9]. The first row transition metals have oxidation state dependent toxicity [10]. Manganese has an interesting chemistry of multiple oxidation states. Being essential nutrition, manganese helps in the production of glucose and the feeding of mitochondria during its maintenance [11]. However, Mn in +2 oxidation state predominates in cellular toxicity [12]. Immoderate exposure of Mn²⁺ causes “Manganism”, which is neurodegenerative disorder which leads to neuronal death [13]. Some general effects of manganese toxicity are memory loss, insomnia, headache, and speech disturbances [14]. Similarly, iron is a good biocatalyst but it also has harmful effects [15]. A high

concentration of tissue iron causes numerous pathological states such as heart disease, diabetes, abnormality in immune system and liver disorders [16]. Similarly, Fe^{2+} (ferrous ion) is highly poisonous and has corrosive effects on the gastrointestinal mucosa (GI). Nausea, diarrhea, vomiting, and abdominal pain are the outcomes of iron poisoning [17]. Moreover, macromolecules are also destroyed by the free radicals generated by Fe^{2+} in the presence of oxygen, resulting in cell death [18]. Co^{+2} is likely to be more dangerous than Co^{+3} . The ultimate effects of cobalt toxicity in a +2 oxidation state are fever, gastrointestinal distress, heart failure, inflammation, and low thyroid level [19]. According to The International Agency for Research on Cancer (IARC), the risk of cancer from cobalt toxicity is about 30% [20]. Copper acts as a component of allosteric the enzyme and is used in the production of a variety of neurotransmitters [21]. Copper in a +2 oxidation state is associated with liver damage, Wilson disease and insomnia [22]. Excessive intake of copper has adverse toxicological complications. Lost cognition is also observed due to a high copper intake in the general population [23]. The notable functions of zinc in humans include proliferation, protein synthesis, neuronal growth, DNA metabolism, free radical sequestration, cellular division and lipid peroxidation [24]. Zn^{+2} is considered toxic when a surplus amount of it is ingested into the body [25]. An elevated risk of prostatic cancer is caused by high doses of zinc [26]. On the contrary, if the toxicity of chromium is extremely interrelated with its oxidation state, it will be highly toxic if the state of oxidation is higher, and vice versa. Cr^{+6} is the sturdiest oxidizing agent and is considered to be 1000 times more dangerous than chromium in a +3 oxidation state [27]. Chromium is cancer-causing metal; its toxicity is not only accessible to humans—plants and animals are also heavily affected by its consumption [28]. Different surfaces are used for the detection, adsorption, and removal of transition metals in different oxidation states; however, the selectivity of a particular metal in the presence of other transition metals is a challenge. Various sensing materials are used for their detection, including kaolinite, magnetite, polyphenol acetaldehyde resins, activated carbon, graphene oxide, picolinamide (Pi-A)-decorated reduced-graphene oxide (RGO), etc. [29–34] Here, we are using a C_2N nanosheet which is already employed as an electrochemical sensor for the detection of toxic and hazardous organic compounds such as HCN , H_2S , PH_3 , HF , NCl_3 , COCl_2 , NCl_3 , NBr_3 , NH_3 , NI_3 and NF_3 [35]. Additionally C_2N has shown its high efficacy in the field of optics, batteries, gas sensors and photo catalysis [36]. To the best of our knowledge, the nitrogenated holey graphene nanosheet has not been previously adopted as an electrochemical sensor for transition metals. The C_2N nanosheet has periodic geometry with standard pore size. C_2N comprises a highly electron-rich cavity consisting of benzene and pyrazine rings alternatively attached. The pyrazine ring of C_2N provides us with highly electronegative nitrogen, which coheres to and catches transition metals.

Our theoretical study provides valuable insight into the unique properties of the C_2N nanosheet and its potential applications as a sensor. However, we also acknowledge that experimental studies are required to validate our theoretical findings and to address the practical challenges associated with the use of C_2N nanosheets, for example, improving the structural stability of C_2N nanosheets is crucial for their long-term use, as they can be unstable under certain conditions, such as high temperature or when exposed to moisture. Developing methods for the precise control of the size and thickness of C_2N nanosheets is important for optimizing their properties and performance. Controlling and minimizing defects and impurities in the structure of C_2N nanosheets is crucial for improving their chemical and electronic properties, as well as their overall performance. While carbon and nitrogen are generally considered non-toxic, the potential toxicity of C_2N nanosheets is not well understood. Further research is needed to determine any adverse effects of C_2N on human health and the environment. It is important to handle and use C_2N nanosheets with caution and follow the appropriate safety guidelines to minimize the potential risks.

2. Results and Discussion

2.1. Geometric Optimization

The structure of the cluster model of the nitrogenated holey graphene (C_2N) nanosheet is shown in Figure 1. A single unit of a C_2N nanosheet comprises nitrogen atoms which are arranged in a periodical manner to set up a ring diameter of 8.30 Å. The pyrazine ring of C_2N provided us with highly electronegative nitrogen which acts as an extremely powerful part, cohering and adsorbing toxic transition metals. The single monolayer of C_2N reflects four possible sites for the adsorption of analytes: (a) in the middle of C_2N surface (A), (b) in the middle of nitrogen atoms (B), (c) above the pyrazine ring (C), and (d) above the benzene ring (D). To find the most stable geometry with the lowest energy for each $TM@C_2N$ complex, all possible orientations of each metal ion over carbon nitride surface were explored. All the complexes ($Cu^{2+}@C_2N$, $Mn^{2+}@C_2N$, $Co^{2+}@C_2N$, $Fe^{2+}@C_2N$, $Cr^{6+}@C_2N$, $Zn^{2+}@C_2N$) exhibited the best performance in the central position, i.e., position (A), as it was the most stable and had the lowest energy (Figure 2).

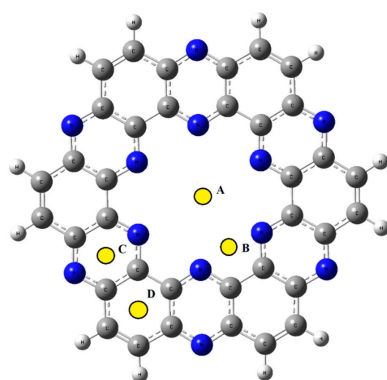


Figure 1. Optimized structure and available adsorption sites of C_2N surface. A–D shows four possible sites for the adsorption of analytes.

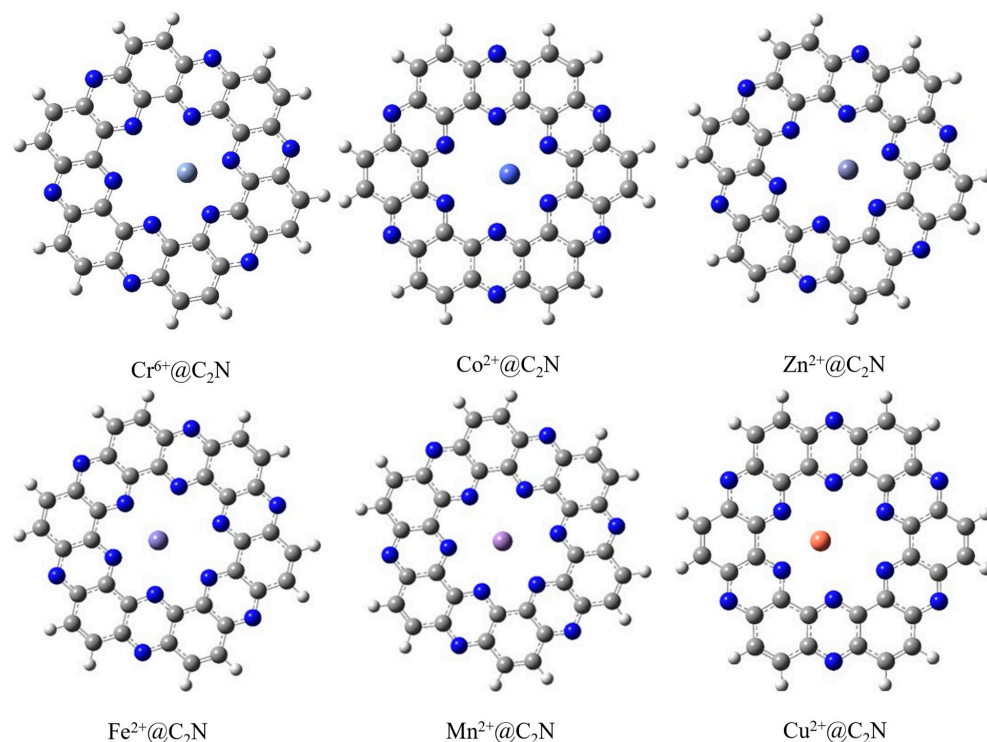


Figure 2. The most stable configuration of $TM@C_2N$ complexes ($Cr^{6+}@C_2N$, $Co^{2+}@C_2N$, $Zn^{2+}@C_2N$, $Fe^{2+}@C_2N$, $Mn^{2+}@C_2N$ and $Cu^{2+}@C_2N$).

2.2. Most Stable Spin State of TM@C₂N Complexes

In this study, the analytes selected for sensing studies were six metals of a first-row transition series (Cu²⁺, Mn²⁺, Fe²⁺, Zn²⁺, Cr⁶⁺ and Co²⁺). First, it was essential to determine the most stable spin state of the TM@C₂N complexes. The optimization of Cu@C₂N, Mn@C₂N and Co@C₂N was carried out in doublet, quartet, sextet, and octet spin states. The relative energies of different spin states for all the complexes are given in Table 1. The most stable spin states obtained for Cu@C₂N, Mn@C₂N and Co@C₂N were doublet, sextet, and quartet spin states, respectively. Similarly, the rest of metal complexes, such as Fe@C₂N, Cr@C₂N and Zn@C₂N, showed quintet, triplet and singlet spin states to the most stable states, respectively.

Table 1. Relative energies in kcal mol^{−1} for the spin states of TM@C₂N complexes.

Spin States	Complexes		
	Cu ²⁺ @C ₂ N	Co ²⁺ @C ₂ N	Mn ²⁺ @C ₂ N
Doublet	0.0	23	68
Quartet	37	0.0	69
Sextet	85	41	0.0
Octet	136	89	46
	Cr ⁶⁺ @C ₂ N	Fe ²⁺ @C ₂ N	Zn ²⁺ @C ₂ N
Singlet	80	60	0.0
Triplet	0.0	21	28
Quintet	0.4	0.0	29
Septet	6.8	35	30

2.3. Interaction Energies

The interaction energies and interaction distances of all the complexes are given in Table 2. In all the complexes, the transition metal interacts with N-atoms of the C₂N cavity (Figure 3). The value of interaction energy of the Cu²⁺@C₂N complex is the lowest among all the studied complexes, i.e., −6.6 kcal mol^{−1} along with 2.2 Å of interaction distance between closest interacting (Cu-62 ... N-47) atoms. The E_{int} and D_{int} (Cr-61 ... N-34) in the Cr⁶⁺@C₂N complex are −9.2 kcal mol^{−1} and 2.09 Å, respectively. In the case of Zn²⁺@C₂N, Fe²⁺@C₂N and Co²⁺@C₂N complexes, the E_{int} is −15.9, −25.9 and −20.7 kcal mol^{−1}, respectively. The interaction energy of Mn²⁺@C₂N (−43.1 kcal mol^{−1}) is greater than the rest of the five complexes showing chemisorption; it interacts at site A of the C₂N cavity with an interaction distance of 2.34 Å.

Table 2. Interaction energies (kcal mol^{−1}) of the most stable TM@C₂N complexes.

TM@C ₂ N (Solvent = Water)	Interaction Energy (kcal mol ^{−1})	Interacting Atoms	Interaction Distance (Å)
Cu ²⁺ @C ₂ N (Doublet)	−6.6	Cu-61 N-47	2.21
Cr ⁶⁺ @C ₂ N (Quintet)	−9.2	Cr-61 N-34	2.09
Zn ²⁺ @C ₂ N (Singlet)	−15.9	Zn-61 N-47	2.12
Co ²⁺ @C ₂ N (Quartet)	−20.7	Co-61 N-34	2.20
Fe ²⁺ @C ₂ N (Sextet)	−25.9	Fe-61 N-47	2.30
Mn ²⁺ @C ₂ N (Triplet)	−43.1	Mn-61 N-47	2.34

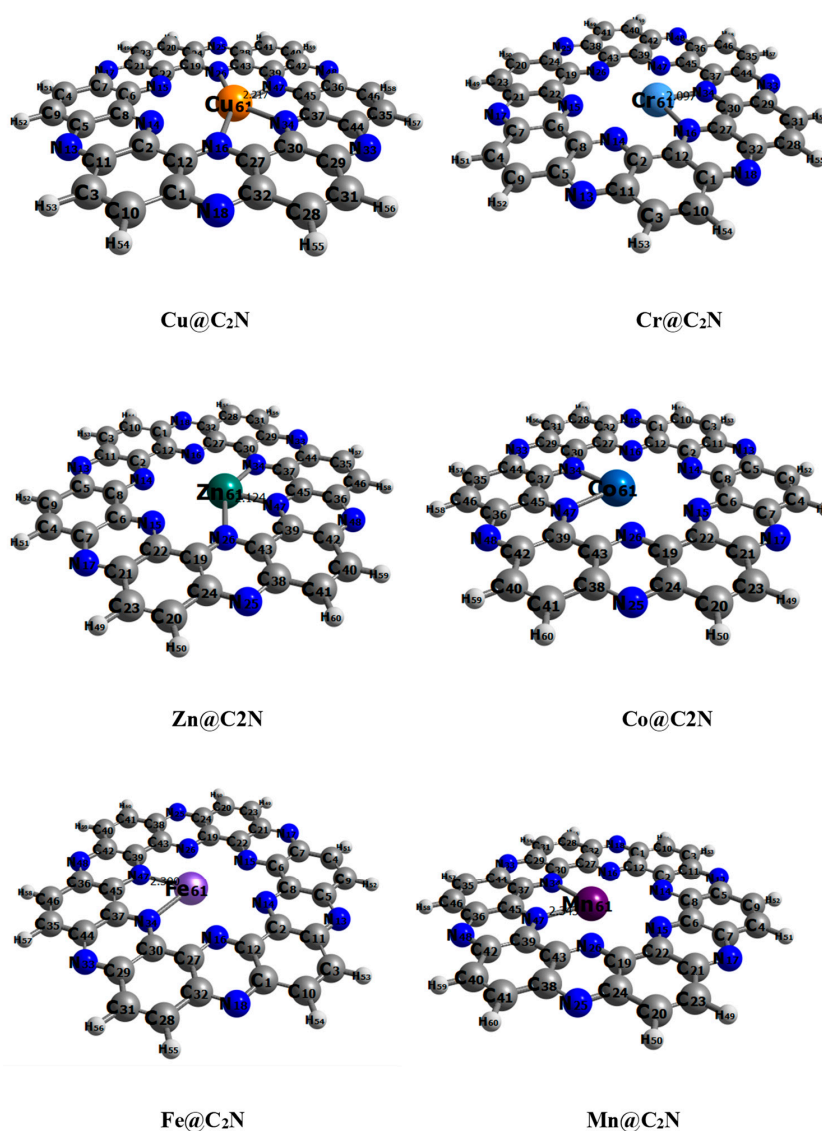


Figure 3. The closest interaction distances D_{int} for TM@C₂N complexes.

The interaction energy results of the TM@C₂N complexes support the existence of a physisorption mechanism, except for Mn@C₂N and Fe²⁺@C₂N which show chemisorption. The interaction energy trends observed for TM@C₂N complexes are Cu@C₂N > Cr@C₂N > Zn@C₂N > Co@C₂N > Fe@C₂N > Mn@C₂N, respectively. The results of the interaction energy indicate that C₂N can accommodate transition metals on its surface, but the highest interaction energy was seen for the Mn@C₂N complex (−43.1 kcal mol^{−1}).

2.4. Natural Bond Orbital Analysis (NBO)

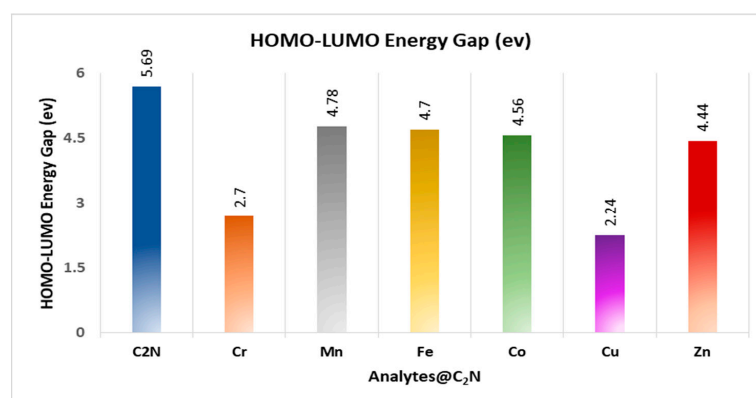
The analysis of natural bond orbital reveals the ability of the sensor to detect the toxic transition metals. The transfer of charge, as well as the direction of charge transfer, was determined using NBO analysis. The calculated charge transfer is listed in Table 3. The transfer of charge may occur from C₂N to metal or metal to C₂N. In this study, the charge values on adsorbed metals are 0.871 |e| (Cu), 1.640 |e| (Fe), 1.672 |e| (Mn), 1.652 |e| (Zn), 0.861 |e| (Co) and 1.79 |e| (Cr). The Q_{NBO} values of TM@C₂N complexes show that charges shifted from analytes (transition metals) to the C₂N nanosheet, as evidenced by the highly electron-rich cavity of C₂N (due to the presence of electronegative nitrogen) and the positive charge of the metals. The following order of charge transfer was observed in the complexes: Cr⁶⁺@C₂N > Mn²⁺@C₂N > Zn²⁺@C₂N > Fe²⁺@C₂N > Cu²⁺@C₂N > Co²⁺@C₂N.

Table 3. The E_{HOMO} , E_{LUMO} , $E_{\text{H-L}}$ gap (in eV) of $\text{TM@C}_2\text{N}$ complexes and charges on metals $|e|$.

Complexes	E_{HOMO}	E_{LUMO}	$E_{\text{H-L}}$ (eV)	Q_{NBO}
C_2N	−7.870	−2.17	5.71	-
$\text{Cu}^{2+}\text{@C}_2\text{N}$	−13.30	−11.06	2.24	0.871
$\text{Fe}^{2+}\text{@C}_2\text{N}$	−13.22	−8.51	4.71	1.640
$\text{Mn}^{2+}\text{@C}_2\text{N}$	−13.27	−8.48	4.80	1.672
$\text{Zn}^{2+}\text{@C}_2\text{N}$	−13.17	−8.73	4.44	1.652
$\text{Cr}^{6+}\text{@C}_2\text{N}$	−24.05	−21.35	2.70	1.79
$\text{Co}^{2+}\text{@C}_2\text{N}$	−13.20	−8.637	4.56	0.861

2.5. Frontier Molecular Orbital Analysis (FMO)

The reactivity of interacting substances is significantly defined by frontier molecular orbital analysis (FMO). The energy gap obtained by taking the difference between the highest occupied molecular orbital (HOMO) and the lowest unoccupied molecular orbitals (LUMO) greatly influences the conductivity as well as the stability of complexes. The E_{HOMO} and E_{LUMO} of C_2N are −7.87 eV and −2.17 eV, respectively. The H–L energy gap in C_2N is 5.71 eV. In $\text{TM@C}_2\text{N}$ complexes, the H–L energy gap reduced to 2.24 eV (Cu), 4.71 eV (Fe), 4.80 eV (Mn), 4.44 eV (Zn), 2.70 (Cr) and 4.56 eV (Co) as graphically represented in Figure 4. In the $\text{Cu@C}_2\text{N}$ complex, HOMO and LUMO energies were −13.3 eV and −11.06 eV, respectively. A moderate reduction in H–L energy gap was observed for the complexes of Fe, Mn, and Co, i.e., 4.71, 4.80 and 4.56 eV, respectively. However, a remarkable decrease was observed in the $E_{\text{H-L}}$ energy gap of $\text{Cu}^{2+}\text{@C}_2\text{N}$ (2.24 eV), which indicates the increased conductivity and sensitivity of C_2N towards copper. Similarly, the LUMO (−21.35 eV) and HOMO (−24.05) of $\text{Cr}^{6+}\text{@C}_2\text{N}$ were more highly stabilized compared to the bare C_2N unit (−2.17 eV, −7.870 eV), which caused a notable decrease in the H–L energy gap (2.70 eV). The notable decrease in the $E_{\text{H-L}}$ gap evidences the greater sensitivity of C_2N towards copper and chromium. The appreciable downfall in the HOMO–LUMO energy gap of any substances represents its appreciable sensitivity and selectivity towards toxic transition metals. Moreover, the orbital densities are also analyzed to visualize the interaction behavior of transition metals and the C_2N surface (Figure 5). All the complexes show totally different orbital densities for LUMO. Except for manganese, the densities of LUMO for the rest of complexes were distributed at different half portions of the C_2N cavity. In case of $\text{Mn@C}_2\text{N}$, the LUMO was entirely located on manganese metal at the center of cavity, whereas the density of HOMO was present as seen in the C_2N unit. The highest decline in the H–L energy gap was observed in the $\text{Cu@C}_2\text{N}$ having the maximum conductivity. Therefore, Cu tends to enhance the conductivity of the carbon nitride surface as compared to the other selected metals.

**Figure 4.** Graphical representation of H–L gap of $\text{TM@C}_2\text{N}$.

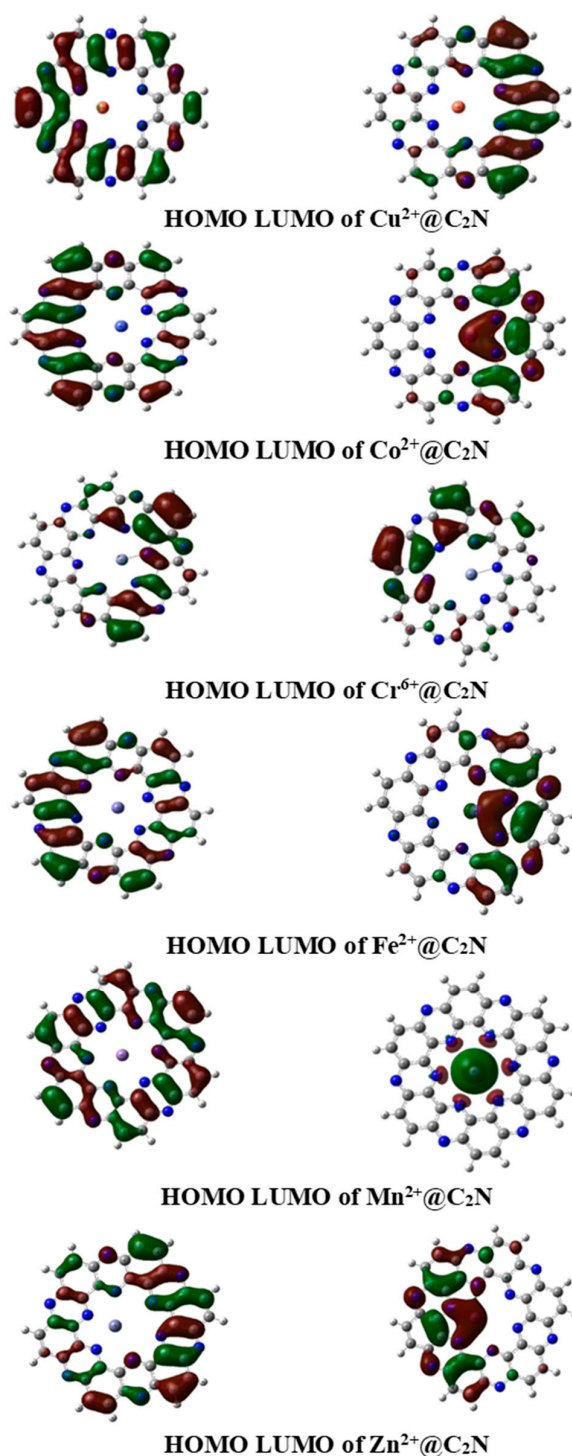


Figure 5. 3D isosurfaces of HOMO and LUMO of TM@C₂N complexes.

2.6. Non-Covalent Interactions (NCI)

NCI analysis reveals the nature of interactions between the analyte and the surface through RDG graphs and 3D isosurfaces. The RDG graph is based on the following equation:

$$\text{RDG}(s) = \frac{1}{2(3\pi^2)^{\frac{1}{3}}} \frac{\nabla\rho}{\rho^{\frac{4}{3}}}$$

where $\nabla\rho$ and ρ are electronic density gradient and electronic density, respectively. The color scheme of NCI graphs comprises different types of interactions; the steric repulsion

is reported in the red color, while weak and strong interactions are represented by the green and blue colors, respectively. In the 3D isosurfaces of all the TM@C₂N complexes, the patches of interactions are mainly shown in the middle part, i.e., the center of the ring; the dotted patches reflect weak interactions, whereas the thicker patches show the strong interactions. In all TM@C₂N complexes, the appearance of green surfaces of different intensities between the metals and C₂N surface indicates the existence of strong and weak van der Waals interactions. In all the complexes, steric clashes are observed from the presence of thicker patches of red color; these repulsive forces are observed due to the presence of the delocalized electrons present in the metals as well as the nitrogen atom of the pyrazine rings. In RDG plots as shown in the Figure 6, the TM@C₂N presents a variety of greenish peaks between -0.02 and 0.01 a.u. A dispersive light-bluish and the greenish spike (nearly -0.02 a.u.) implies the presence of strong non-bonding interactions.

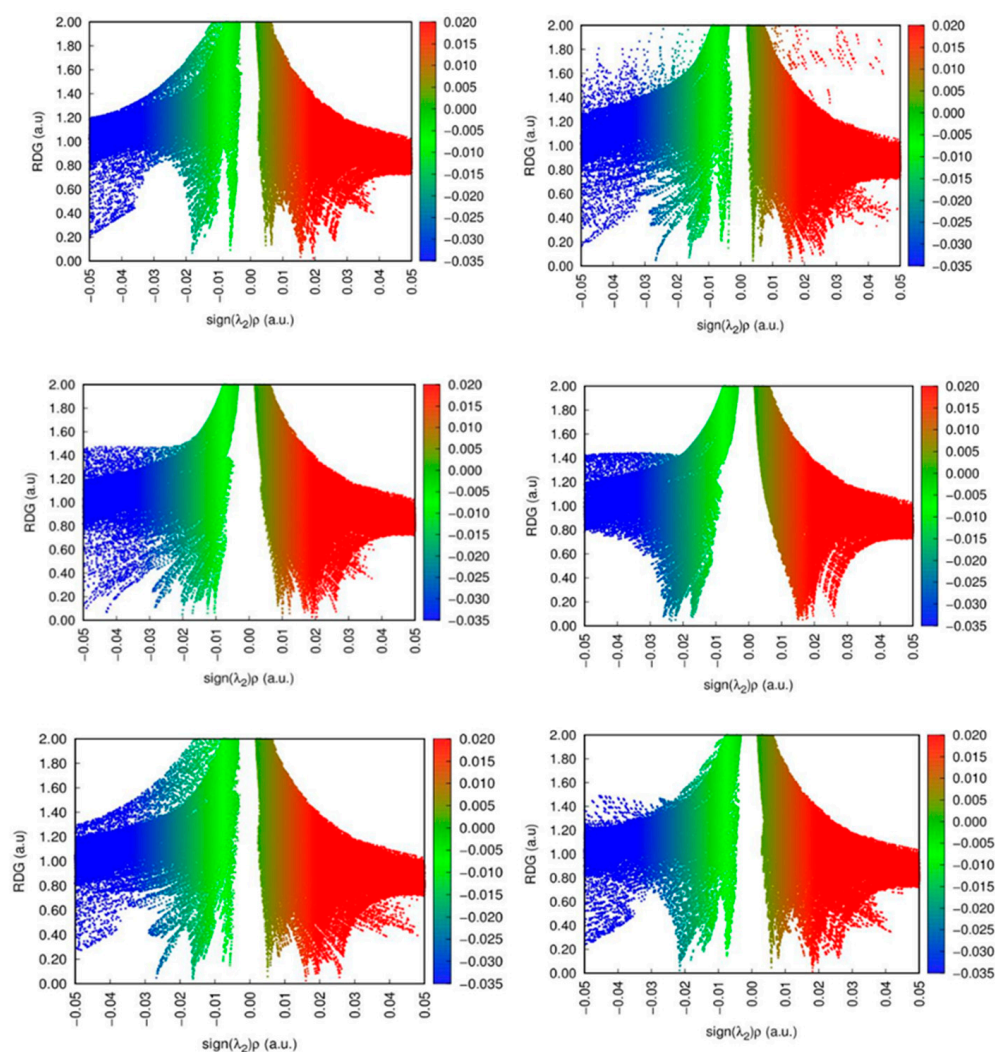


Figure 6. 2D RDG graphs of TM@C₂N complexes (Cr⁶⁺@C₂N, Co²⁺@C₂N, Zn²⁺@C₂N, Fe²⁺@C₂N, Mn²⁺@C₂N and Cu²⁺@C₂N).

2.7. QTAIM Analysis

In QTAIM analysis, the bond nature between analyte and complex depends on bond-critical point (BCP). BCP's are further classified into five components, i.e., electronic density (ρ), potential energy density $V(r)$, energy density $H(r)$, Laplacian of electron density ($\nabla^2 \rho$)

and kinetic energy density $G(r)$. The bond-critical point (BCP) can be more distantly elucidated by the following equation:

$$H(r) = G(r) + V(r)$$

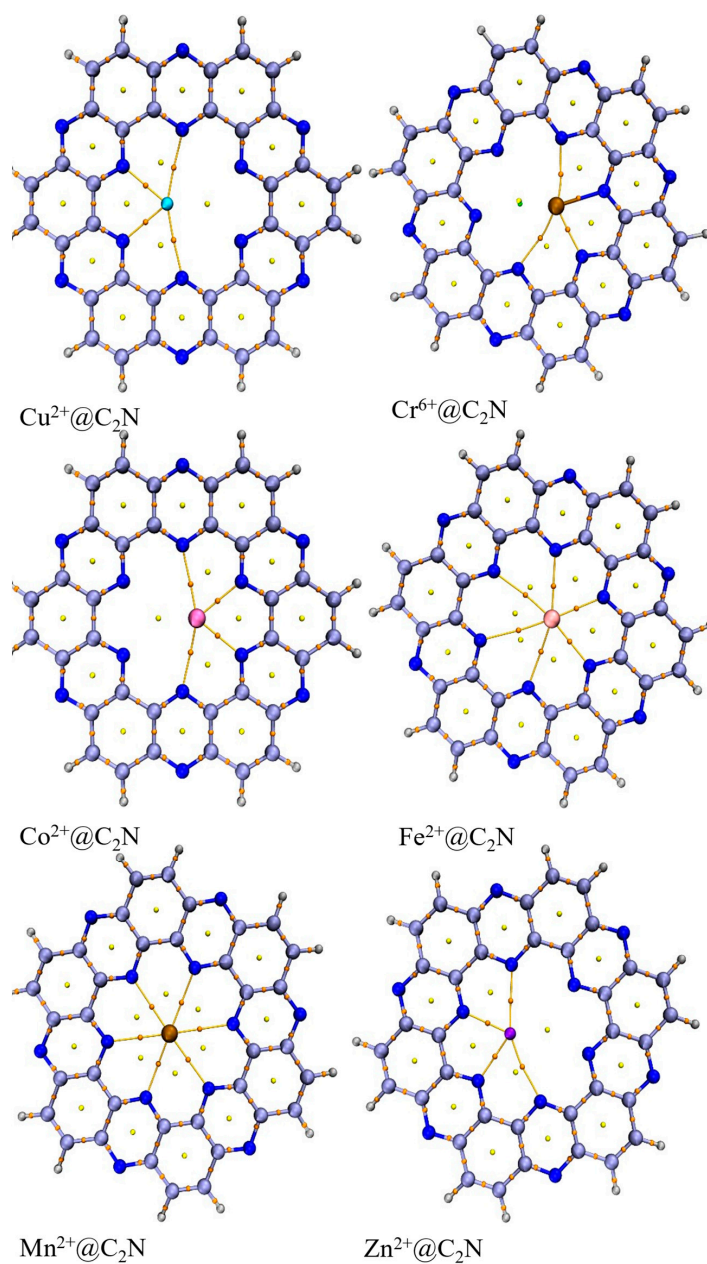
which shows that the sum of the potential energy and kinetic energy density is equal to the electron density. The value of $H(r) > 0$ and $H(r) < 0$ indicates the presence of closed-shell and shared-shell interactions, respectively. The bond-critical point (BCP) results of electronic density (ρ) and Laplacian ($\nabla^2 \rho$) are given in Table 4 and the BCPs are depicted in Figure 7. The geometry of $\text{Cu@C}_2\text{N}$ complexes consists of four BCPs. The bond-critical point values of ρ ranges from 0.02 to 0.05 a.u. and $\nabla^2 \rho$ from 0.07 to 0.19 a.u. Among four BCPs values, two interactions (N23 — Cu30 and N36 — Cu30 of C_2N and Cu) contain the highest value of electronic density (ρ), 0.05 a.u. In $\text{Cu@C}_2\text{N}$, the values of electronic density (ρ) are less than 0.1, which indicate the presence of weak van der Waals interactions, as confirmed by a 3D isosurface of an NCI plot. The highest number of BCPs obtained among the studied systems was six in the cases of $\text{Fe}^{2+}\text{@C}_2\text{N}$ and $\text{Mn}^{2+}\text{@C}_2\text{N}$. The values of 0.02 a.u. to 0.35 a.u. for ρ , and -0.10 a.u. to -0.97 a.u. for $\nabla^2 \rho$, were obtained for $\text{Fe}^{2+}\text{@C}_2\text{N}$. In case of $\text{Fe}^{2+}\text{@C}_2\text{N}$, one of the values of electronic density (ρ) was less than zero, which indicates the existence of electrostatic interactions, as confirmed by SAPT0 analysis. Similarly, the electronic density (ρ) of $\text{Zn}^{2+}\text{@C}_2\text{N}$ (0.2 to 0.4 a.u.) is greater than 0.1, which confirms the electrostatic interactions between zinc and the C_2N nanosheet. For $\text{Cr}^{6+}\text{@C}_2\text{N}$ and $\text{Co}^{2+}\text{@C}_2\text{N}$, the values of electronic density confirm the presence of van der Waals interactions, i.e., $\rho < 0.1$ as confirmed by the greenish patches in the RDG graph. The outcomes of QTAIM analysis were in great accordance with the NCI and SAPT0 analyses.

Table 4. The values of topological parameter of BCPs of $\text{TM@C}_2\text{N}$ complex obtained from QTAIMs analysis.

Analytes@ C_2N	C_2N —Analyte	BCP	ρ	$\nabla^2 \rho$	G (r)	V (r)	H (r)	V(r)/G(r)
$\text{Cu}^{2+}\text{@C}_2\text{N}$	N18-	96	0.02	0.07	0.01	-0.01	0.001	1.0
	N23-	99	0.05	0.19	0.06	-0.08	-0.014	1.3
	N36-	112	0.05	0.19	0.06	-0.07	-0.014	1.1
	N44-	117	0.02	0.07	0.01	-0.04	0.001	4
$\text{Fe}^{2+}\text{@C}_2\text{N}$	N18-	97	0.35	-0.10	0.34	-0.94	-0.59	2.7
	N23-	100	0.33	-0.97	0.11	-0.48	-0.36	4.3
	N25-	104	0.29	-0.78	0.07	-0.34	-0.27	4.8
	N37-	115	0.30	-0.82	0.08	-0.37	-0.29	4.6
	N39-	119	0.34	-0.10	0.31	-0.89	-0.57	2.8
	N-44	122	0.02	0.18	0.04	-0.03	0.008	0.7
$\text{Zn}^{2+}\text{@C}_2\text{N}$	N20-	97	0.40	-0.010	0.34	-0.90	-0.6	2.6
	N21-	101	0.29	-0.779	0.078	-0.35	-0.3	4.4
	N33-	109	0.29	-0.114	0.033	0.35	-0.3	10
	N42-	115	0.302	-0.82	0.086	-0.37	-0.2	4.3
$\text{Mn}^{2+}\text{@C}_2\text{N}$	N19-	97	0.35	-0.10	0.34	-0.94	-0.6	2.7
	N22-	101	0.293	-0.779	0.078	-0.35	-0.3	4.4
	N28-	106	0.292	-0.11	0.032	-0.35	-0.3	11
	N34-	111	0.28	-0.76	0.073	-0.33	-0.3	4.5
	N40-	116	0.33	-0.99	0.122	-0.49	-0.4	4.0
	N43-	120	0.015	0.045	0.010	-0.009	0.008	0.9

Table 4. Cont.

Analytes@C ₂ N	C ₂ N—Analyte	BCP	ρ	$\nabla^2\rho$	G(r)	V(r)	H(r)	V(r)/G(r)
Cr ⁶⁺ @C ₂ N	N18-	94	0.016	0.033	0.010	−0.012	−0.002	1.2
	N23-	97	0.053	0.29	0.071	−0.069	0.003	0.9
	N36-	108	0.069	0.375	0.095	−0.097	−0.002	1.0
	N44-	112	0.026	0.068	0.020	−0.024	0.004	1.2
Co ²⁺ @C ₂ N	N18-	98	0.02	0.05	0.016	−0.019	−0.003	1.1
	N26-	103	0.057	0.18	0.059	−0.072	−0.013	1.2
	N39-	116	0.057	0.18	0.059	−0.072	−0.013	1.2
	N44-	117	0.021	0.0561	0.016	−0.019	−0.002	1.1

Figure 7. The BCPs obtained using a QTAIM analysis of TM@C₂N complexes.

2.8. SAPTO Analysis

Symmetry-adapted perturbation theory (SAPT) provides a quantitative analysis of the noncovalent interaction between two entities through the perturbative approach by directly computing the interaction energy as a perturbation to the Hamiltonian of the individual monomers instead of the supermolecular approach. The division of interaction energy into different components such as dispersion, exchange, electrostatic and induction has been performed using SAPT ($E_{\text{int SAPT}} = E_{\text{elec}} + E_{\text{ind}} + E_{\text{disp}} + E_{\text{exch}}$). The interpretation of SAPTO analysis is helpful for providing an explanation of the nature of interactions between the analytes (metals) and the C₂N unit, and for quantifying the chemical bonds. The interactions of SAPTO for six complexes are shown in Table 5. The components of SAPTO, which are negative, reveal the presence of attractive interactions between the C₂N units and the transition metals. The exchange part contains the positive energies, which indicates the presence of repulsive interactions between the C₂N unit and the analytes. As shown in Table 5, the negative energies of SAPTO among all the complexes (TM@C₂N) denote the presence of attractive interactions. The interaction energies obtained in SAPTO studies of metal complexes were -255.09 kcal/mol (Cu²⁺@C₂N), -131.88 kcal/mol (Fe²⁺@C₂N), -283.35 kcal/mol (Mn²⁺@C₂N), -306.20 kcal/mol (Zn²⁺@C₂N), -174 kcal/mol (Co²⁺@C₂N) and -5145.7 kcal/mol (Cr⁶⁺@C₂N). The highest contribution towards the total SAPTO was observed for E_{elec} . Hence, electrostatic interactions dominate and stabilize the complexes. The findings of the SAPTO analysis are consistent with the NCI and QTAIM analyses. The trend in supermolecular interaction energy (without solvent) is exactly followed by the E_{SAPTO} . The trend for E_{SAPTO} is Cr@C₂N > Zn@C₂N > Mn@C₂N > Cu@C₂N > Co@C₂N < Fe@C₂N.

Table 5. The SAPTO analysis (in kcal mol⁻¹) of TM@C₂N complexes.

TM@C ₂ N	E_{elec}	E_{exch}	E_{Ind}	E_{disp}	E_{SAPTO}
Cu ²⁺ @C ₂ N	-167.46	41.33	-121.82	-7.15	-255.09
Fe ²⁺ @C ₂ N	-163.28	38.03	0.3244	-6.96	-131.88
Mn ²⁺ @C ₂ N	-156.84	24.55	-144.44	-6.62	-283.35
Zn ²⁺ @C ₂ N	-173.33	45.06	-170.61	-7.31	-306.20
Co ²⁺ @C ₂ N	-172.68	54.46	-48.38	-7.82	-174.43
Cr ⁶⁺ @C ₂ N	-463.26	81.73	-4759.46	-4.76	-5145.76

2.9. Electrical Conductivity and Sensitivity Analysis

Electrical conductivity (σ) is calculated for pristine C₂N and TM@C₂N complexes at 300 K and the σ values are given in Table 6. The conductivity of TM@C₂N complexes show a marked increase as compared to pristine C₂N. In particular, Cu²⁺@C₂N and Cr⁶⁺@C₂N conductivities increase largely when compared to other TM@C₂N complexes. This large increase in conductivity can be converted to an electrical signal. Therefore, it can be concluded that the nitrogenated holey graphene C₂N may be a promising electronic sensor for the detection of Cu and Cr. To further confirm the higher sensitivity of C₂N towards toxic transition metals, the sensing characteristics of C₂N were quantitatively analyzed using a sensitivity (S) test. Sensitivity is the response of a sensor towards analyte exposure. A high value of S means the material is an excellent sensor for the particular analyte. The sensitivity of the C₂N nanosheet is found to be 142.63, 10.79, 0.09, 0.69, 107.30, and 51.90 towards Cu, Fe, Mn, Zn, Cr, and Co, respectively. Cu adsorbed on the C₂N complex shows the highest S value, which indicates that among the mixture of analytes, C₂N is the most sensitive and selective towards Cu.

Table 6. Work function (Φ), sensitivity S (%), and conductivity (σ) values of TM@C₂N complexes.

Complexes	Φ	S (%)	σ
C ₂ N	5.02	-	1.09×10^{-48}
Cu ²⁺ @C ₂ N	12.18	142.63	1.53×10^{-19}
Fe ²⁺ @C ₂ N	10.86	10.79	2.74×10^{-40}
Mn ²⁺ @C ₂ N	10.87	0.09	4.80×10^{-41}
Zn ²⁺ @C ₂ N	10.95	0.69	5.08×10^{-38}
Cr ⁶⁺ @C ₂ N	22.7	107.30	2.09×10^{-23}
Co ²⁺ @C ₂ N	10.92	51.90	4.98×10^{-39}

3. Computational Methodology

The level of theory employed for geometry optimization is M05-2X/6-31+G (d, p) [37,38]. In our investigation of C₂N–transition metal complexes, non-covalent interactions are involved, and therefore, we have employed the hybrid meta-exchange-correlation functional M05-2X. The choice of M05-2X functional is based on its accuracy in describing non-covalent interactions, as demonstrated by benchmark studies such as the one by Burns et al. [39] and other studies reported in the literature on the non-covalent interactions [40–43]. Additionally, the choice of an appropriate basis set is a crucial factor in computational simulations. To this end, we have utilized the double zeta basis set 6-31+G(d,p), which includes diffuse and polarized functions and strikes a balance between accuracy and computational efficiency [44]. The interaction energies between C₂N and transition metals were calculated by using the following equation:

$$E_{int} = E_{TM@C_2N} - (E_{C_2N} + E_{TM})$$

where $E_{TM@C_2N}$, E_{C_2N} and E_{TM} are the interaction energies of C₂N–transition metal complexes, pristine C₂N surface, and isolated transition metal, respectively. To find the lowest energy structure, each metal is placed in different possible orientations and the results are visualized using Gaussview 5.0 [45]. To validate the true minima's nature of the TM@C₂N complexes, vibrational frequencies were examined for the presence of imaginary frequencies. An NCI analysis was carried out using VMD and Multiwfn software for an improved evaluation of the interactive sites between C₂N and the selected transition metals [46,47]. The electronic properties, such as the natural bond orbital (NBO) and frontier molecular orbital (FMO) analyses, were performed at the same level of theory used for optimization. The non-covalent interactions between C₂N and transition metals were quantified by bond-critical point using QTAIM analysis [48]. The interaction energies between transition metals and the C₂N nanosheet were also analyzed using SAPT0 (symmetry-adaptation perturbation theory). SAPT0 analysis illustrates four types of interactions: electrostatic (ΔE_{elst}), exchange (ΔE_{exh}), induction (ΔE_{ind}) and dispersion (ΔE_{dis}) [49]. The equation for ΔE_{int} through SAPT0 is as follows:

$$\Delta E_{int} = \Delta E_{elst} + \Delta E_{exh} + \Delta E_{ind} + \Delta E_{dis}$$

All the SAPT calculations were performed using PSI4 1.6 software [50].

4. Conclusions

This study aimed to systematically investigate the ability of a two-dimensional nitrogenated holey graphene (C₂N) nanosheet to detect toxic transition metals (Cu²⁺, Mn²⁺, Fe²⁺, Zn²⁺, Cr⁶⁺, and Co²⁺) using DFT calculations. The interaction energies between C₂N and each of the transition metals were calculated, with values of −6.6, −43.1, −20.7, −25.9, −9.2, and −15.9 kcal mol^{−1} for Cu²⁺@C₂N, Mn²⁺@C₂N, Co²⁺@C₂N, Fe²⁺@C₂N, Cr⁶⁺@C₂N, and Zn²⁺@C₂N, respectively. These results suggest that the adsorption of the transition metals on C₂N is mainly due to physisorption, except for Mn and Fe, which are

chemisorbed. The dominant interaction between C₂N and the metals was found to be the electrostatic force of attraction, which stabilizes the TM@C₂N complexes. The computed E_{H-L} gap of the C₂N nanosheet was found to decrease significantly upon the adsorption of Cu²⁺ and Cr⁶⁺. The NCI plots and QTAIM analysis showed the presence of strong and weak van der Waals interactions between C₂N and the metals. The increase in the electrical conductivity of Cu²⁺@C₂N and Cr⁶⁺@C₂N, as compared to the pristine C₂N, indicates the superior sensitivity of C₂N towards these metals. The sensitivity (S) test also confirms the higher sensitivity and selectivity of C₂N towards Cu²⁺. In conclusion, the results of this study suggest that the two-dimensional nitrogenated holey graphene (C₂N) nanosheet could be an effective sensor for detecting copper (II) and hexavalent chromium. The findings may also provide valuable insights into the design and development of sensors for detecting other toxic metals.

Author Contributions: Conceptualization, U.S. and F.U.; Data curation, U.S. and N.H.B.Z.A.; Formal analysis, N.H.B.Z.A. and M.H.S.A.H.; Funding acquisition, N.S.S.; Methodology, U.S. and F.U.; Project administration, N.S.S.; Resources, T.M.; Software, F.U.; Supervision, K.A.; Validation, T.M.; Visualization, M.H.S.A.H.; Writing—original draft, U.S. and F.U.; Writing—review and editing, K.A. All authors have read and agreed to the published version of the manuscript.

Funding: FIC research grant and allied research grant, Universiti Brunei Darussalam (UBD/RSCH/1.4/FICBF(b)/2022/049).

Institutional Review Board Statement: Not applicable.

Informed Consent Statement: Not applicable.

Data Availability Statement: All data are provided in the manuscript.

Acknowledgments: The authors thank the Universiti Brunei Darussalam for the FIC research grant (UBD/RSCH/1.4/FICBF(b)/2022/049) and the allied research grant.

Conflicts of Interest: The authors declare no conflict of interest.

References

1. Pareek, B.; Singh, V.; Sharma, V.; Singh, P.S. Properties of Transition Metals and Their Compounds. *Contemp. Adv. Sci. Technol.* **2021**, *1*, 146.
2. Hossain, M.R.; Hasan, M.M.; Nishat, M.; Noor, E.A.; Ahmed, F.; Ferdous, T.; Hossain, M.A. DFT and QTAIM investigations of the adsorption of chlormethine anticancer drug on the exterior surface of pristine and transition metal functionalized boron nitride fullerene. *J. Mol. Liq.* **2021**, *323*, 114627. [[CrossRef](#)]
3. El-Gammal, O.A.; El-Bindary, A.A.; Mohamed, F.S.; Rezk, G.N.; El-Bindary, M.A. Synthesis, characterization, design, molecular docking, anti COVID-19 activity, DFT calculations of novel Schiff base with some transition metal complexes. *J. Mol. Liq.* **2022**, *346*, 117850. [[CrossRef](#)]
4. Bönemann, H.; Brijoux, W.; Brinkmann, R.; Joußen, T.; Korall, B.; Dinjus, E. Formation of colloidal transition metals in organic phases and their application in catalysis. *Angew. Chem. Int. Ed. Engl.* **1991**, *30*, 1312–1314. [[CrossRef](#)]
5. Ullah, F.; Ayub, K.; Mahmood, T. High performance SACs for HER process using late first-row transition metals anchored on graphyne support: A DFT insight. *Int. J. Hydrogen Energy* **2021**, *46*, 37814–37823. [[CrossRef](#)]
6. O'Halloran, T.V. Transition metals in control of gene expression. *Science* **1993**, *261*, 715–725. [[CrossRef](#)]
7. Huang, Y.W.; Wu, C.H.; Aronstam, R.S. Toxicity of Transition Metal Oxide Nanoparticles: Recent Insights from in vitro Studies. *Materials* **2010**, *3*, 4842–4859. [[CrossRef](#)]
8. Crans, D.C.; Kostenkova, K. Open questions on the biological roles of first-row transition metals. *Commun. Chem.* **2020**, *3*, 104. [[CrossRef](#)]
9. Mills, K.C.; Curry, S.C. Acute iron poisoning. *Emerg. Med. Clin. N. Am.* **1994**, *12*, 397–413. [[CrossRef](#)]
10. Van Cleave, C.; Crans, D.C. The first-row transition metals in the periodic table of medicine. *Inorganics* **2019**, *7*, 111. [[CrossRef](#)]
11. Reaney, S.H.; Kwik-Urbe, C.L.; Smith, D.R. Manganese oxidation state and its implications for toxicity. *Chem. Res. Toxicol.* **2002**, *15*, 1119–1126. [[CrossRef](#)]
12. Erikson, K.M.; Syversen, T.; Aschner, J.L.; Aschner, M. Interactions between excessive manganese exposures and dietary iron-deficiency in neurodegeneration. *Environ. Toxicol. Pharmacol.* **2005**, *19*, 415–421. [[CrossRef](#)]
13. Crossgrove, J.; Zheng, W. Manganese toxicity upon overexposure. *NMR Biomed.* **2004**, *17*, 544–553. [[CrossRef](#)]
14. McMillan, D. A brief history of the neurobehavioral toxicity of manganese: Some unanswered questions. *Neurotoxicology* **1999**, *20*, 499–507.

15. Dias, A.M.; Hussain, A.; Marcos, A.S.; Roque, A.C. A biotechnological perspective on the application of iron oxide magnetic colloids modified with polysaccharides. *Biotechnol. Adv.* **2011**, *29*, 142–155. [[CrossRef](#)]
16. Fraga, C.G.; Oteiza, P.I. Iron toxicity and antioxidant nutrients. *Toxicology* **2002**, *180*, 23–32. [[CrossRef](#)]
17. Chamnongpol, S.; Dodson, W.; Cromie, M.J.; Harris, Z.L.; Groisman, E.A. Fe(III)-mediated cellular toxicity. *Mol. Microbiol.* **2002**, *45*, 711–719. [[CrossRef](#)]
18. Britton, R.S.; Leicester, K.L.; Bacon, B.R. Iron toxicity and chelation therapy. *Int. J. Hematol.* **2002**, *76*, 219–228. [[CrossRef](#)]
19. Leyssens, L.; Vinck, B.; Van Der Straeten, C.; Wuyts, F.; Maes, L. Cobalt toxicity in humans—A review of the potential sources and systemic health effects. *Toxicology* **2017**, *387*, 43–56. [[CrossRef](#)]
20. Suh, M.; Thompson, C.M.; Brorby, G.P.; Mittal, L.; Proctor, D.M. Inhalation cancer risk assessment of cobalt metal. *Regul. Toxicol. Pharm.* **2016**, *79*, 74–82. [[CrossRef](#)]
21. Kaim, W.; Rall, J. Copper—A “modern” bioelement. *Angew. Chem. Int. Ed. Engl.* **1996**, *35*, 43–60. [[CrossRef](#)]
22. Tisato, F.; Marzano, C.; Porchia, M.; Pellei, M.; Santini, C. Copper in diseases and treatments, and copper-based anticancer strategies. *Med. Res. Rev.* **2010**, *30*, 708–749. [[CrossRef](#)] [[PubMed](#)]
23. Uriu-Adams, J.Y.; Keen, C.L. Copper, oxidative stress, and human health. *Mol. Asp. Med.* **2005**, *26*, 268–298. [[CrossRef](#)] [[PubMed](#)]
24. Frassinetti, S.; Bronzetti, G.; Caltavuturo, L.; Cini, M.; Croce, C.D. The role of zinc in life: A review. *J. Env. Pathol. Toxicol. Oncol.* **2006**, *25*, 597–610. [[CrossRef](#)]
25. Beyersmann, D. Homeostasis and cellular functions of zinc. *Materialwiss. Werkstofftech.* **2002**, *33*, 764–769. [[CrossRef](#)]
26. Tudor, R.; Zalewski, P.D.; Ratnaik, R.N. Zinc in health and chronic disease. *J. Nutr. Health Aging* **2005**, *9*, 45–51.
27. Shekhawat, K.; Chatterjee, S.; Joshi, B. Chromium toxicity and its health hazards. *Int. J. Adv. Res* **2015**, *3*, 167–172.
28. Guertin, J. Toxicity and health effects of chromium (all oxidation states). In *Chromium (VI) Handbook*; CRC Press: Boca Raton, FL, USA, 2004; pp. 215–234. [[CrossRef](#)]
29. Gu, X.; Evans, L.J. Surface complexation modelling of Cd (II), Cu (II), Ni (II), Pb (II) and Zn (II) adsorption onto kaolinite. *Geochim. Cosmochim. Acta* **2008**, *72*, 267–276. [[CrossRef](#)]
30. Mulani, K.; Daniels, S.; Rajdeo, K.; Tambe, S.; Chavan, N. Adsorption of chromium (VI) from aqueous solutions by coffee polyphenol-formaldehyde/acetalddehyde resins. *J. Polym.* **2013**, *2013*, 98368. [[CrossRef](#)]
31. Saha, B.; Tai, M.; Streat, M. Adsorption of transition metals from aqueous solutions by modified activated carbons. *Chem. Eng. Res. Des.* **2003**, *81*, 1343–1353. [[CrossRef](#)]
32. White, R.L.; White, C.M.; Turgut, H.; Massoud, A.; Tian, Z.R. Comparative studies on copper adsorption by graphene oxide and functionalized graphene oxide nanoparticles. *J. Taiwan Inst. Chem. Eng.* **2018**, *85*, 18–28. [[CrossRef](#)]
33. Yang, L.; Huang, N.; Huang, L.; Liu, M.; Li, H.; Zhang, Y.; Yao, S. An electrochemical sensor for highly sensitive detection of copper ions based on a new molecular probe Pi-A decorated on graphene. *Anal. Methods* **2017**, *9*, 618–624. [[CrossRef](#)]
34. Das, B.; Ghosh, A.; Dorairaj, D.P.; Dolai, M.; Karvembu, R.; Mabhai, S.; Im, H.; Dey, S.; Jana, A.; Misra, A. Multiple ion (Al³⁺, Cr³⁺, Fe³⁺, and Cu²⁺) sensing using a cell-compatible rhodamine-phenolphthalein-derived Schiff-base probe. *J. Mol. Liq.* **2022**, *354*, 118824. [[CrossRef](#)]
35. Yar, M.; Hashmi, M.A.; Khan, A.; Ayub, K. Carbon nitride 2-D surface as a highly selective electrochemical sensor for V-series nerve agents. *J. Mol. Liq.* **2020**, *311*, 113357. [[CrossRef](#)]
36. Yar, M.; Hashmi, M.A.; Ayub, K. The C 2 N surface as a highly selective sensor for the detection of nitrogen iodide from a mixture of NX 3 (X = Cl, Br, I) explosives. *RSC Adv.* **2020**, *10*, 31997–32010. [[CrossRef](#)]
37. Csonka, G. Proper basis set for quantum mechanical studies of potential energy surfaces of carbohydrates. *J. Mol. Struct. Theochem.* **2002**, *584*, 1–4. [[CrossRef](#)]
38. Zhao, Y.; Schultz, N.E.; Truhlar, D.G. Design of Density Functionals by Combining the Method of Constraint Satisfaction with Parametrization for Thermochemistry, Thermochemical Kinetics, and Noncovalent Interactions. *J. Chem. Theory Comput.* **2006**, *2*, 364–382. [[CrossRef](#)]
39. Burns, L.A.; Vazquez-Mayagoitia, A.; Sumpter, B.G.; Sherrill, C.D. Density-functional approaches to noncovalent interactions: A comparison of dispersion corrections (DFT-D), exchange-hole dipole moment (XDM) theory, and specialized functionals. *J. Chem. Phys.* **2011**, *134*, 084107. [[CrossRef](#)]
40. Hohenstein, E.G.; Chill, S.T.; Sherrill, C.D. Assessment of the Performance of the M05-2X and M06-2X Exchange-Correlation Functionals for Noncovalent Interactions in Biomolecules. *J. Chem. Theory. Comput.* **2008**, *4*, 1996–2000. [[CrossRef](#)]
41. Goel, S.; Masunov, A.E. Dissociation curves and binding energies of diatomic transition metal carbides from density functional theory. *Int. J. Quantum Chem.* **2011**, *111*, 4276–4287. [[CrossRef](#)]
42. Malloum, A.; Conradie, J. Structures, binding energies and non-covalent interactions of furan clusters. *J. Mol. Graph. Model.* **2022**, *111*, 108102. [[CrossRef](#)] [[PubMed](#)]
43. Zhao, Y.; Truhlar, D.G. Applications and validations of the Minnesota density functionals. *Chem. Phys. Lett.* **2011**, *502*, 1–13. [[CrossRef](#)]
44. Elm, J.; Mikkelsen, K.V. Computational approaches for efficiently modelling of small atmospheric clusters. *Chem. Phys. Lett.* **2014**, *615*, 26–29. [[CrossRef](#)]
45. Li, W.; Xie, H.; Huang, Y.; Song, L.; Shao, Y.; Qiu, K. Application of Gaussian 09/GaussView 5.0 in analytical chemistry teaching. *J. Kunming Med. Univ.* **2016**, *134*–136.
46. Lu, T.; Chen, F. Multiwfn: A multifunctional wavefunction analyzer. *J. Comput. Chem.* **2012**, *33*, 580–592. [[CrossRef](#)]

47. Johnson, E.R.; Keinan, S.; Mori-Sanchez, P.; Contreras-Garcia, J.; Cohen, A.J.; Yang, W. Revealing noncovalent interactions. *J. Am. Chem. Soc.* **2010**, *132*, 6498–6506. [[CrossRef](#)]
48. Vega, D.; Almeida, D. AIM-UC: An application for QTAIM analysis. *J. Comput. Methods Sci. Eng.* **2014**, *14*, 131–136. [[CrossRef](#)]
49. Hohenstein, E.G.; Sherrill, C.D. Density fitting of intramonomer correlation effects in symmetry-adapted perturbation theory. *J. Chem. Phys.* **2010**, *133*, 014101. [[CrossRef](#)]
50. Smith, D.G.A.; Burns, L.A.; Simmonett, A.C.; Parrish, R.M.; Schieber, M.C.; Galvelis, R.; Kraus, P.; Kruse, H.; Di Remigio, R.; Alenaizan, A.; et al. Psi4 1.4: Open-source software for high-throughput quantum chemistry. *J. Chem. Phys.* **2020**, *152*, 184108. [[CrossRef](#)]

Disclaimer/Publisher’s Note: The statements, opinions and data contained in all publications are solely those of the individual author(s) and contributor(s) and not of MDPI and/or the editor(s). MDPI and/or the editor(s) disclaim responsibility for any injury to people or property resulting from any ideas, methods, instructions or products referred to in the content.